Enhanced Turbulence associated with the Diurnal Jet in the Ocean Surface Boundary Layer

Graig Sutherland*

Department of Mathematics, University of Oslo, Norway

School of Physics and the Ryan Institute, National University of Ireland, Galway

Louis Marié

Laboratoire de Physique des Océans, CNRS/IFREMER/IRD/UBO, Plouzané, France

Gilles Reverdin

LOCEAN Laboratory, Sorbonne Universités (UPMC, University of Paris 6)-CNRS-IRD-MNHN, Paris, France

Kai H. Christensen

Norwegian Meteorological Institute, Oslo, Norway

Göran Broström

Department of Earth Sciences, University of Göteborg, Göteborg, Sweden

Brian Ward

School of Physics and the Ryan Institute, National University of Ireland, Galway

Corresponding author address: Department of Mathematics, University of Oslo, Postboks 1053
Blindern, 0316 Oslo, Norway
E-mail: graigors@math.uio.no

ABSTRACT

Microstructure observations of the upper ocean in the subtropical Atlantic are obtained with the Air-Sea Interaction Profiler (ASIP), an autonomous upwardly rising profiler designed to observe the ocean surface boundary layer (OSBL). Under conditions of relatively low winds and high solar insolation, the turbulent dissipation rate (ε) in the upper few metres is observed to increase during daytime restratification. This enhanced ε is associated with the diurnal jet, which forms during the day due to the wind stress input being restricted to the shallow reformed OSBL. The high shear layer is associated with the active mixing layer depth (XLD), which reforms in the early morning about 3 hours before a density based mixed layer depth (MLD), causing the generation of shear instabilities. The diurnal jet is simulated using a damped slab model with observed values of the wind stress input as well as the time varying OSBL depth. The model shows the diurnal jet to generate shear instabilities for relatively small wind speeds with these instabilities occurring within a couple of hours after OSBL reformation.

1. Introduction

Many processes in the ocean surface boundary layer (OSBL) vary with the diurnal forcing of daily heating and nightly cooling, with this response being more pronounced at lower latitudes where high levels of solar insolation are a dominant feature. The most notable of these cycles is the diurnal variability of sea surface temperature (SST) which has long been observed and relatively well studied (e.g. Ward 2006). Under conditions of low winds and high solar radiation, the diurnal variability of SST has been shown to be an important component to the air-sea fluxes on climatological timescales in subtropical regions (Bernie et al. 2005; Kawai and Wada 2007; Clayson and Bogdanoff 2013). In addition to SST, diurnal variability has also been observed in sea surface salinity (Drushka et al. 2014; Asher et al. 2014), momentum and shear (Weller and Plueddemann 1996; Plueddemann and Weller 1999; Cronin and Kessler 2009; Weller et al. 2014) and biogeochemical tracers such as dissolved oxygen and chlorophyll (Nicholson et al. 2015). In comparison, the diurnal variability of turbulence has received far less attention although it is a key physical component the OSBL.

The primary mechanism for turbulence generation in the OSBL is the wind, either directly through the wind stress at the ocean surface or indirectly through waves (e.g. Sutherland et al. 2013; D'Asaro 2014). The wind variability over the open ocean is expected to be primarily occurring on synoptic time scales and is not expected to greatly impact diurnal variability in turbulence. In addition to the wind forcing, a buoyancy flux due to the daily cycle of heating/cooling between the atmosphere and ocean acts to enhance/restrict turbulence in the OSBL. These buoyancy fluxes have a large diurnal signal in subtropical regions.

Increased stratification has a tendency to restrict turbulent motions as they quickly dampen due to the restoring force of gravity. This damping effect has been observed in the OSBL during restratification with a decrease in the dissipation rate of turbulent kinetic energy (ε) of an order of magnitude or more compared to wind scaling (Brainerd and Gregg 1993; Vagle et al. 2012). The increased stratification also acts to limit the vertical transport of the wind stress input which acts to enhance near surface shear (Cronin and Kessler 2009). This phenomenon has been referred to as a diurnal jet (Price et al. 1986) or slippery seas (Woods and Strass 1986; Kudryavtsev and Soloviev 1990) where the observed daytime currents are greater than expected for a shear layer adjacent to a solid boundary. Diurnal jets have been observed in regions with high insolation and typically form in the upper few metres with velocities $\mathscr{O}(10 \text{ cm s}^{-1})$ (Price et al. 1986; Callaghan et al. 2014).

This paper aims to address the near surface turbulent processes which are impacted by diurnal restratification in the OSBL. Section 2 provides an overview of diurnal processes in the OSBL. Data and methods are presented in section 3. The diurnal structure of the observations are investigated by using a composite day, which is calculated by phase averaging the forcing and response as a function of the local time of day in section 4. Section 5 presents observations of the near surface velocity structure and explores possible generation mechanisms for the diurnal jet and near-inertial waves in the OSBL. A summary and discussion of the results are presented in section 6.

2. Overview of OSBL dynamics

The diurnal evolution of the OSBL follows the varying buoyancy flux between solar heating during the day and surface cooling during the night. A schematic of this diurnal cycle is depicted in Fig. 1. The general cycle has been described in some detail previously (e.g. Lombardo and Gregg 1989; Callaghan et al. 2014).

An important length scale in the OSBL dynamics is the Monin-Obukhov length (Large et al. 1994), which has traditionally been used as a stability parameter for boundary layers. The Monin-Obukhov length (L) is the approximate depth where wind forcing balances the buoyancy production,

$$L = -\frac{u_*^3}{\kappa B_0}, \tag{1}$$

where u_* is the friction velocity, B_0 is the surface buoyancy fluxán constant and κ is the von Kármán constant and is equal to 0.4. The Monin-Obukhov length underpins similarity theory, which assumes that OSBL dynamics can be written as universal functions of the stability parameter H/L, where H is the OSBL depth. This length scale has been very effective in unstable regimes where nighttime cooling acts to destabilize the water column and enhance turbulence (Shay and Gregg 1986; Lombardo and Gregg 1989), with slight modifications such as non-local forcing due to the buoyancy flux being applied only at the surface (Large et al. 1994), and enhanced mixing due to surface gravity waves (Belcher et al. 2012; Sutherland et al. 2014a; Callaghan et al. 2014).

Similarity theory is not as effective during diurnal restratification when B_0 is stabilizing. Shortwave radiation can penetrate tens of metres, which is much greater than the OSBL depth during restratification, and B_0 leads to an overestimate of the buoyancy production and hence underestimates L. It is expected that only the shortwave radiation absorbed in the mixed layer will contribute to stability, although this depth could be shallower (Large et al. 1994). For shallow mixed layers this requires accurate information about the attenuation of shortwave radiation in the upper ocean.

Under moderate to low winds (1) may also underestimate the OSBL depth if there is enhanced turbulence arising from shear instabilities generated by the trapping of near surface momentum due to stratification. Enhanced shear has been shown to generate in the morning in the absence of cyclic behaviour in the wind stress (Smyth et al. 2013), suggestive of a buoyancy generated phenomenon.

3. Data and Methods

Observations in the OSBL were obtained during the SubTRopical Atlantic Surface Salinity Experiment (STRASSE) aboard the N/O *Thalassa* (Reverdin et al. 2015). This experiment took place during August and September 2012 as part of the larger Salinity Processes in the Upper Ocean Regional Study (SPURS) project. The location of the experiment is shown in Fig. 2. The latitude of the experiment site is about 25.6°N, which corresponds to an inertial period of 27.7 hours.

a. Meteorological Observations

Radiative fluxes and wind speed measurements were recorded aboard the N/O *Thalassa*. The wind stress and buoyancy flux were calculated using the TOGA COARE 3.0 algorithm (Fairall et al. 2003). Figure 3a shows the 10-metre wind speed U_{10}, direction U_{DIR} and surface buoyancy flux B_0. The wind speed varied over a range from 2-10 m s^{-1} with directions ranging between predominantly from the north to easterly. The surface buoyancy flux (B_0) followed a typical pattern of surface cooling at night and heating during the day.

b. Wave and Current Observations

Observations of surface gravity waves and velocity profiles were made with a cloverleaf buoy (Trèfle) equipped with a downward-facing RDI 300 kHz ADCP, an xSens MTI-G GPS / motion sensor package, and a Nortek Vector velocimeter. The buoy was tethered to a 50 m-drogued SVP drifter in order to reduce its windage-induced drift. A custom data logger performed collection and consistent time stamping of the three data streams. The ADCP profiled from 3.5 to 103.5 m with a 1 m depth resolution, and an effective range of roughly 75 m.

Wave motions were quantified using the xSens MTI-G GPS motion sensor package, which consists of a GPS and a 6 degrees of freedom inertial motion unit (IMU) sampled at 10 Hz. The GPS and IMU comprise an Attitude Heading Reference System (AHRS) which uses a Kalman filter to combine the inertial motions and GPS coordinates.

The vertical motion was subsequently band pass filtered using a fourth order Chebyshev type II filter with a 40 dB stop band ripple and cutoff frequencies 0.025 Hz and 3 Hz, applied forwards and then backwards to eliminate phase delay, resulting in an eighth order, 80 dB ripple filter. Wave spectra were calculated every 30 minutes from the AHRS heave. The calculated significant wave height H_s, peak period T_p, and zero up-crossing period T_z are shown in Fig. 3b.

The surface Stokes velocity was calculated from the 1-D wave spectra (Kenyon 1969) as

$$u_{s0} = \frac{16\pi^3}{g} \int_{f_{min}}^{f_{max}} f^3 S(f) df \tag{2}$$

where $S(f)$ is the 1-D wave spectrum and f_{min} and f_{max} are the cut-off frequencies chosen as 0.05 and 0.50 Hz respectively. There are two opposing uncertainties with calculating the Stokes velocity from a 1-D wave spectra using a finite frequency range: the lack of a measured high frequency spectral tail and the lack of the directional spreading of the wave energy. The former will lead to a systematic underestimate of u_{s0} up to 30% (Rascle et al. 2006), with the exact amount dependent on the slope of the spectral tail, while the latter leads to a systematic overestimate of u_{s0} up to 30%, (Webb and Fox-Kemper 2011) dependent on the directional spread of wave energy. Lacking measurements of both the high frequency component of the wave spectrum and directional information, we assume that the two should approximately cancel each other. Note that these assumptions could lead to a maximum uncertainty in u_{s0} of 30%, but that the true error is most likely much less. This band pass filter approach is identical to that used by Gargett and Grosch (2014) and Sutherland et al. (2014a), and has been found to be a good determinate for the surface Stokes velocity.

The surface Stokes velocity is used in conjunction with the friction velocity $u_* = \sqrt{\tau/\rho}$ to calculate the turbulent Langmuir number $\mathrm{La} = \sqrt{u_*/u_{s0}}$, which is often used as a proxy for turbulence associated with Langmuir circulations (McWilliams et al. 1997). Here τ is the wind stress and ρ is the density of sea water. Figure 3c shows values for u_{s0}, u_* and La. Langmuir circulations are expected for $\mathrm{La} < 0.3$ (McWilliams et al. 1997), which is not fulfilled during our observations. We therefore assume Langmuir circulations to not be a dominant mechanism in our observations.

Near surface velocity measurements are presented relative to a reference depth of 40 m located just below the seasonal mixed layer. Figure 4 shows the mean currents at 40 m along with the velocity anomalies relative to this current. Inertial oscillations dominate the velocity variability in the OSBL. Enhanced near surface shear is seen to form every day, consistent with the diurnal jet phenomenon described by Price et al. (1986).

c. Microstructure Measurements

Measurements of the turbulent dissipation rate, temperature and salinity were obtained with ASIP. A total of 347 profiles from 40 metres depth were made over 5 ASIP deployments with each deployment ranging from 24 to 48 hours in duration with the exception of the fifth deployment which was only 10 hours. The time between successive profiles for each deployment was about 20 minutes.

The time-depth evolution of temperature, T, and buoyancy frequency, N^2, is shown in Fig. 5. The density ratio in the OSBL, defined by $R_\rho = \alpha T_z / \beta S_z$, where α and β are the thermal expansion coefficient and the saline contraction coefficient respectively and T_z and S_z are the vertical gradients of temperature and salinity respectively, is typically greater than 2 indicative of temperature controlled stratification. In addition, the conductivity signal, from which salinity is calculated, in the upper metre is sometimes contaminated from the impact of near-surface detritus striking the conductivity probe, which acts to increase the noise in the measured salinity. Therefore, only the contribution from T_z is used to calculate N^2 in the OSBL.

Dissipation rates of turbulent kinetic energy, ε, were measured using two airfoil shear probes mounted on the front of ASIP (Sutherland et al. 2013). Assuming isotropic turbulence allows ε to be calculated using $\varepsilon = 7.5\nu \left\langle u_z'^2 \right\rangle$, where ν is the kinematic viscosity and u_z' is the turbulent vertical shear. The turbulent vertical shear u_z' was sampled at 1000 Hz and vertical profiles were divided into 1 second segments where the power spectral density was calculated using Welch's method. The mean rise velocity of ASIP is 0.5 m s^{-1} thus giving a vertical resolution of 0.5 m. Details of the processing algorithm for ε can be found in Ward et al. (2014). Figure 5c shows the measured turbulent dissipation rate for the five deployments.

In addition, Fig. 5d shows ε normalized by

$$\varepsilon_0 = a\frac{u_*^3}{\kappa|z|}. \tag{3}$$

Equation (3) is the expected dissipation profile for a constant stress layer adjacent to a rigid boundary. The constant a is chosen such that mean profiles of $\varepsilon/\varepsilon_0$ are on average equal to 1, which for this data set corresponds to $a = 0.4$. Although there are expected to be deviations in the vertical structure of ε relative to ε_0 (e.g. Terray et al. 1996), for the bulk of the OSBL it has been shown that $\varepsilon \approx \varepsilon_0$ (Sutherland et al. 2013; Callaghan et al. 2014). Deviations from (3) are expected to arrive from wave effects, such as wave breaking and Langmuir circulations, but such effects are ignored here since La is typically greater than the expected threshold of 0.3 for Langmuir circulations to develop (McWilliams et al. 1997). In this data set, enhanced dissipation in the wave affected region is not expected to be a function of the local time of day as the wave field varies on much slower time scales (see Fig. 3).

When the surface buoyancy forcing is destabilizing, there is a depth-independent enhancement of ε proportional to B_0 (Lombardo and Gregg 1989; Callaghan et al. 2014) which is omitted in (3). Rather than introduce another empirical constant for the convective contribution to ε, this term is omitted as it will be much less than ε_0 in the near surface region. Neglecting the buoyancy term leads to $\varepsilon > \varepsilon_0$ during the night at depths where ε is comparable to B_0, generally greater than 10 m, as can be seen in Fig. 5d.

The mixed layer depth, MLD, is calculated using two temperature thresholds, the accepted value of 0.2°C (Kara et al. 2000; de Boyer Montégut et al. 2004) and a smaller threshold of 0.1°C which may be more applicable to variations observed over a diurnal cycle. These two MLDs will be denoted $\mathrm{MLD}_{0.2}$ and $\mathrm{MLD}_{0.1}$ for each threshold used. Both MLD definitions are calculated relative to the temperature at $z_r = 0.5$ m. The MLDs over the five ASIP deployments are shown by the grey lines in Fig. 5. The active mixing layer depth, XLD, is defined as the depth where ε decreases to a background level of 10^{-9} $\mathrm{m^2s^{-3}}$. This threshold was found to be optimal for buoyancy driven conditions (Sutherland et al. 2014b) and consistent within an order of magnitude with previous definitions for the XLD (Lozovatsky et al. 2006; Fer and Sundfjord 2007). Differences between the MLD and XLD have been shown to be important in resolving observations of ε with surface forcing (Brainerd and Gregg 1995; Stevens et al. 2011; Sutherland et al. 2014a). The XLD is shown by the black line in Fig. 5.

Mean values for the day and night profiles of $\varepsilon/\varepsilon_0$, temperature, and current speed is shown in Figure 6. The mean day profile is defined as the mean from 13:00-16:00 local mean time (LMT) and the night as the mean between 01:00-04:00 LMT. Local mean time is calculated such that noon coincides with the peak solar altitude. During the night, similarity theory appears to hold as $\varepsilon/\varepsilon_0 = 1$, while during the day there are large deviations from this. The near surface ratio $\varepsilon/\varepsilon_0$ is greater during the day than at night. This enhancement occurs over the upper 5 metres and appears to be associated with the near surface increase in current (Fig. 6c).

4. Composite Day

Due to the slow variation in the wind and wave fields it is convenient to phase average the forcing and response components as functions of the LMT to create a single composite day. This allows for a detailed analysis of the mean response of the ocean to diurnal forcing while filtering out processes which are expected to be more stochastic, such as the waves and wind. This method has been shown to be a useful technique in regions with strong buoyancy forcing (Smyth et al. 2013; Drushka et al. 2014; Sutherland et al. 2014b).

Figure 7 shows the composite day for the surface forcing and ocean parameters. The phase averaging is performed for hourly bins, with depths averaged over 1 metre bins. The phase averaged surface buoyancy flux B_0 and wind speed U_{10} are shown in Fig. 7a. The diurnal structure of the surface buoyancy flux varies little over the observed period. Although the wind speed varies from 2 to 10 m s^{-1} over all the deployments, there is no distinct diurnal structure to the variability with the phase averaged wind speed equal to 5.8 ± 0.6 m s^{-1} over the day (Fig. 7a).

The near surface stratification, (N^2, Fig. 7b), and shear squared (S^2, Fig. 7c), both show an increase at about 09:00 LMT, with N^2 lagging S^2 by a few hours. Both N^2 and S^2 reach near surface maxima at about 14:00 LMT at which point the shear and stratification descend to greater depths. In the afternoon as the depth of the OSBL increases, the magnitude of N^2 and S^2 both decrease.

As an indicator for shear stability, the gradient Richardson number is calculated,

$$\mathrm{Ri} = \frac{N^2}{S^2}, \tag{4}$$

where N^2 and S^2 are composite day values, similar to Smyth et al. (2013). When Ri falls below a critical value, typically assumed to be 0.25, the flow is expected to become unstable (e.g. Miles 1961). Figure 7d shows the logarithm of Ri centred on $\log_{10} 0.25 = -0.60$ such that the red values corresponds to where shear instability is expected to develop. Figure 7 only shows Ri in stratified regions where $N^2 > 10^{-5}$ s^{-1}. The near surface region satisfies the criterion for shear instability at all times during the high restratification during the day.

The turbulent dissipation rate ε (Fig. 7e) and normalized $\varepsilon/\varepsilon_0$ (Fig. 7f) show the previously observed pattern of ε extending to the base of the seasonal pycnocline during the night and a rapid reduction below 10 metres due to the increased stratification present during the day. However, in the near surface region there is an enhancement in dissipation which begins after 12:00 LMT, roughly 3 hours after the reforming of a shallow mixing layer, and persists for approximately 3 hours.

The MLDs and XLD, shown in Fig. 7, are calculated from the composite values of temperature and dissipation in Fig. 7. The MLDs and XLD are approximately equal during the night while the mixing layer with the 0.2°C threshold reforms during the day approximately 4 hours before the reformation of the mixed layer. This time difference is reduced by nearly half using the smaller threshold of 0.1°C, but giving an MLD much shallower than the XLD during the day. In order to obtain comparable minimum depths between the MLD and XLD a larger ΔT than 0.2°C would have to be used. It may be that the mixing time scales are insufficient to overcome the stabilizing buoyancy flux in order to create a well mixed surface layer.

5. Diurnal Jet

Figure 9 shows the near surface velocity measured at 0.5 m depth relative to the velocity at 20 m. The reference depth of 20 m is chosen as it is below the shallow reformed layer but safely less than the maximum OSBL depth. A clear diurnal signal is observed with the upper velocity bin showing a diurnal pattern with a magnitude of about 0.20 m s^{-1}. The diurnal jet in Fig. 9 demonstrates a similar pattern with the along wind component leading the onset of the near surface shear. The relative magnitudes of the along and cross wind components vary over the deployments with cross wind component starting to dominate during deployments 2 and 3.

a. Damped slab model

To simulate the diurnal jet the OSBL is modelled as a damped slab (Pollard and Millard 1970; D'Asaro 1985; Alford 2001; Mellor 2001) forced by the observed wind stress and OSBL depth. Modelling the OSBL as a homogeneous slab allows for the omission of complicated mixing parameterizations as this is integrated in the observed OSBL depth. Inertial currents in the upper ocean have been relatively well reproduced with such a model (D'Asaro 1985; Alford 2001).

Modelling the OSBL as a slab of depth H forced by a surface stress $i\tau$, where τ is real, the time evolution of the surface current is written as

$$\frac{\partial Z}{\partial t} + \omega Z = \frac{i\tau}{\rho H} \tag{5}$$

where $Z = u + iv$ is the vertically averaged complex current in the mixed layer, and $\omega = r + if$ is a complex damping term where the real part comprises the linear damping coefficient r, which is related to the decay timescale associated with free inertial oscillations, and the imaginary part f is the Coriolis frequency. Complex notation is used for the horizontal components of the flow, with the along-wind direction denoted by the imaginary axis and the cross-wind direction represented by the real axis.

For constant ρ, ω, τ and H, (5) is easily solved for Z giving

$$Z(t) = \frac{i\tau}{\rho\omega H}\left\{1 + \left[Z(0)\frac{\rho\omega H}{\tau} - 1\right]e^{-\omega t}\right\}. \tag{6}$$

Although H is observed to vary significantly over a diurnal cycle, for small values of t, at the onset of the diurnal jet, it is reasonable to assume τ and H to be constant. Equation (6) provides some insight into the initial generation of the diurnal jet, which will be explored in the following section.

b. No Rotation: diurnal jet generation

Assuming $\omega t \ll 1$ and setting the initial condition $Z(0) = 0$, since the jet and the underlying layer will have the same velocity at $t = 0$, (6) can be written as

$$Z(t) = \frac{i\tau t}{\rho H}\left[1 + \mathcal{O}(\omega t)^2\right]. \tag{7}$$

Equation (7) states that the diurnal jet will initially increase linearly with time in the along wind direction and is independent of rotation and the linear damping rate.

To determine the stability of (7), the bulk Richardson number is calculated for the entire OSBL as

$$\mathrm{Ri}_b = \frac{g\Delta\rho}{H\rho}\frac{H^4\rho^2}{\tau^2 t^2} = \frac{g\rho\Delta\rho H^3}{\tau^2 t^2}, \tag{8}$$

where $\Delta\rho$ is the density difference over the OSBL depth H. Shear instability is expected to occur when $\mathrm{Ri}_b < \mathrm{Ri}_{\mathrm{cr}}$ where $\mathrm{Ri}_{\mathrm{cr}} = 0.65$ (Price et al. 1986). Solving for $\mathrm{Ri}_b = \mathrm{Ri}_{\mathrm{cr}}$ in (8) gives an estimate of the time that the mixed layer will remain stable, i.e.

$$t_{\mathrm{cr}} = \left(\frac{g\rho\Delta\rho H^3}{\mathrm{Ri}_{\mathrm{cr}}\tau^2}\right)^{\frac{1}{2}}. \tag{9}$$

Figure 10 shows t_{cr} as a function of H and τ assuming $\Delta\rho = 0.03$ kg m^{-3} (de Boyer Montégut et al. 2004) and $\rho = 1025$ kg m^{-3}. Equation (9) suggests that for $H < 5$ m, the OSBL will not be stable for more than 1.5 hours at moderate wind speeds ($\tau > 0.06$ N m^{-2}, corresponding to $U_{10} \gtrsim$ 6 m s^{-1}). For very small wind speeds ($U_{10} \lesssim 2$ m s^{-1}, corresponding to $\tau < 0.02$ N m^{-2}), $t_{\mathrm{cr}} > 6$ hours and the assumption that $\omega t << 1$ is no longer valid.

With the approximate lifetime of the shallow layer determined, the magnitude of the diurnal jet can be calculated from (7). In general, the flow does not immediately become turbulent once $\mathrm{Ri}_b < \mathrm{Ri}_{\mathrm{cr}}$ and there is a lag of 2-3 hours between Richardson number instability and the turbulence generated by shear instabilities (Smyth et al. 2013). Substituting a time $t = t_{\mathrm{cr}} + t_0$, where t_0 is the time after the $\mathrm{Ri}_b = \mathrm{Ri}_{\mathrm{cr}}$ and the onset of flow instability, into (7), gives the magnitude of the diurnal jet as

$$\Delta v(t_0) = \frac{\tau}{\rho H}(t_{\mathrm{cr}} + t_0) = \left(\frac{g\Delta\rho H}{\mathrm{Ri}_{\mathrm{cr}}\rho}\right)^{\frac{1}{2}} + \frac{\tau}{\rho H} t_0. \tag{10}$$

Figure 11 shows the diurnal jet $\Delta v(t_0)$ in the $\tau - H$ plane. This model predicts a diurnal jet magnitude between 4 and 15 cm s^{-1} for the observed h and τ values for a range of $0 \leq t_0 \leq 3$ hours. For $t_0 = 0$ we have $\Delta v(0)$ quasi-independent of τ similar to what Price et al. (1986) calculated. However, (10) gives values of $\Delta v(0)$ close to 0.5 m s^{-1}, which is smaller than the observed peak along-wind velocity of 0.10 to 0.15 m s^{-1}. Equation (10) is consistent with observations for values of t_0 between 2 and 3 hours.

c. Rotation: inertial currents

At a latitude of 25.6° the assumption of $\omega t \ll 1$ will only be valid for the first few hours. Therefore, rotation can not be reasonably omitted over the lifetime of the diurnal jet. This is clear from the presence of a large cross-wind velocity component to the diurnal jet as shown in Fig. 9. The time lag of the cross-wind component to the along-wind component is consistent with near-inertial oscillations in the OSBL. Near-inertial oscillations in the OSBL are strongly damped and r is selected as a fraction of f, $r = 0.15f$, which is identical with Alford (2001). This value of r corresponds to a decay time scale of 7.7 days at this latitude.

In the mixed layer, inertial oscillations are generated due to the temporal variability of the wind stress input over the depth of the OSBL (Pollard and Millard 1970; D'Asaro 1985; Alford 2001).

Solutions for the current in the mixed layer are derived from (5) by decomposing the current into Ekman and inertial components, i.e $Z = Z_i + Z_E$. D'Asaro (1985) defines the Ekman component as the solution of (5) under a steady wind and OSBL depth

$$Z_E = \frac{i\tau}{\omega\rho H}. \tag{11}$$

Equation (11) is equivalent to (6), which assumed constant τ and H, as $t \to \infty$ such that $e^{-\omega t} \to 0$.

Substituting $Z = Z_i + Z_E$ into (5) and using the definition (11) gives the time evolution of Z_i:

$$\frac{\partial Z_i}{\partial t} + \omega Z_i = -\frac{i}{\rho\omega}\frac{\partial(\tau/H)}{\partial t} = \frac{i\tau}{\rho\omega H}\left(\frac{1}{H}\frac{\partial H}{\partial t} - \frac{1}{\tau}\frac{\partial \tau}{\partial t}\right). \tag{12}$$

The body force term in (12) is equivalent to the body force in (5), but with a multiplication factor proportional to the normalized temporal variability of H and τ. Equation(12) suggests that it is the difference in relative variability of H and τ which excites inertial oscillations in the mixed layer. Therefore, in subtropical regions where H and τ are relatively small, small variability can be a source for relatively large inertial oscillations in the mixed layer.

Using observed values for τ and H, (5) and (12) are utilized to determine if they can sufficiently reproduce observed near inertial velocities of the OSBL. The variability in τ is insufficient to generate the observed currents (see appendix A) and thus the analysis is focused on the variation in H.

1) Variation in H: MLD vs XLD

The response of (5) is shown in Fig. 12 for three definitions of H:the XLD and two thresholds for the MLD. Both the $\text{MLD}_{0.2}$ and the XLD depth give similar magnitudes as the observed diurnal jet while $\text{MLD}_{0.1}$ overestimates the observations. The timing of the diurnal jet, however, is poorly reproduced by all definitions of H although the XLD performs better than the MLD. Both the modelled onset in the morning and the weakening in the late afternoon lag the observed near surface velocities.

The lag in the morning appears to be related to the reformation of the OSBL depth as the XLD produces currents which begin at nearly the same time as observations. However, currents generated by (5) persist longer into the evening than observations for all definitions of H suggestive of missing dissipative processes in (5) rather than inaccuracies in H.

2) Including entrainment

One process not accounted for using the damped slab model is entrainment of the remnant layer which is cut off from the surface wind input during restratification. The current in the remnant layer should decay as an unforced inertial oscillation while the surface layer velocity increases. When the upper layer descends in the afternoon it mixes with the slower remnant layer, which reduces the near surface velocity.

Adding to (5) an entrainment term to account for the deepening of H into the remnant layer below gives

$$\frac{\partial Z}{\partial t} + \omega Z = \frac{i\tau}{\rho H} + \frac{(\hat{Z} - Z)}{H}\frac{\partial H}{\partial t} \tag{13}$$

$$\frac{\partial \hat{Z}}{\partial t} + \omega \hat{Z} = 0 \tag{14}$$

where $\hat{Z}$ is the complex velocity in the remnant layer. Taking $t = 0$ to be the onset of the OSBL reformation so that $\hat{Z}(0) = Z(0)$ and that the maximum OSBL depth is a constant H_0, then (13) and (14) can be solved analytically giving

$$Z(t) = \frac{i\tau}{\rho\omega H_0}\left[e^{-\omega t} + \frac{H_0}{H}\left(1 - e^{-\omega t}\right)\right] \tag{15}$$

$$\hat{Z}(t) = \frac{i\tau}{\rho\omega H_0}e^{-\omega t}. \tag{16}$$

The details of (15) and (16) can be found in Appendix B. For the diurnal jet, which is the surface layer minus the remnant layer i.e. $Z(t)-\hat{Z}(t)$, one gets the same expression as in (7), i.e.

$$Z(t)-\hat{Z}(t)=\frac{i\tau t}{\rho H}\left[1+\mathscr{O}\left(\omega t\right)^{2}\right]. \tag{17}$$

Equation (17) implies that, at least to first order, that the diurnal jet is independent of rotation and should be in the same direction as τ. Therefore, during the early stages after the OSBL reformation when $\omega t \ll 1$, the diurnal jet will be in the along wind direction and be a linear function of t assuming τ is constant. This along wind genesis of the diurnal jet is generally observed (Fig. 9).

The solution in (15) is sensitive to the rate at which H and τ vary so (13) is evaluated numerically using observed τ, MLDs and XLD for the depth of OSBL, as shown in Fig. 12. This model is more consistent with observations when the OSBL depth is defined using the XLD. Defining the OSBL depth with $\mathrm{MLD}_{0.2}$ leads to a large phase lag in the modelled currents relative to the observed further enforcing the importance of accurately resolving the timing of the OSBL dynamics. Although this phase lag is improved with the smaller threshold $\mathrm{MLD}_{0.1}$ the magnitude of this depth is too small and produces currents much too large.

6. Summary and discussion

High resolution observations of the OSBL from the Air-Sea Interaction Profiler (ASIP) are presented here during the STRASSE cruise in August/September 2012. Winds were predominantly moderate to low which, along with high solar insolation, created several shallow OSBL depths that were sampled with ASIP. In addition to resolving the temperature structure on centimetre scales, ASIP also calculated the turbulent dissipation rate, ε, with a 0.5 m vertical resolution for each profile. Over the duration of 10 days the surface buoyancy flux followed a repeating pattern of cooling at night and heating during the day. This produced a typical heating and cooling cycle in SST, and thus created high near surface shear associated with the increased daily stratification.

There were several large diurnal warming events which created enhanced stratification near the surface and acted to drastically reduce ε below the XLD. Above the XLD, enhanced levels of ε were observed which coincided with a region of increased velocity, i.e. the presence of a diurnal jet. The expected mechanism for the enhanced ε during the day is from the generation of shear instabilities created by the large near surface shear generated during the day (Smyth et al. 2013). Observations of the gradient Richardson number are consistent with the presence of shear instabilities, but other processes arising from a shallow OSBL depth and enhanced shear, e.g. near surface internal wave activity (Wain et al. 2015) and Langmuir circulations (Sutherland et al. 2014a), cannot be ruled out.

A damped slab model (Pollard and Millard 1970; D'Asaro 1985; Alford 2001) was used to simulate the near surface currents from the observed wind stress and boundary layer depths. For time scales on the order of a few hours, such that rotation may be neglected, the analytic solution for the stability of a diurnal jet of constant depth and wind stress was calculated. Except under extremely low wind speeds, the shear associated with these shallow layers was expected to become sub-critical within an hour or two. However, to reproduce observed diurnal jet magnitudes, the shallow OSBL was not expected to become turbulent for another two to three hours after the critical Richardson number was reached. This time lag is consistent with other observations of shear generated instabilities (Smyth et al. 2013).

Various definitions for H were explored in this study using the active mixing layer depth (XLD) determined from profiles of ε falling to an empirical background rate (Stevens et al. 2011; Sutherland et al. 2014b), and the mixed layer depth (MLD) determined using a standard temperature threshold of 0.2°C difference from the near surface value (de Boyer Montégut et al. 2004) and a smaller threshold of 0.1°C which may be more applicable to a diurnal cycle. The XLD and $\mathrm{MLD}_{0.2}$ gave similar magnitudes for the diurnal jet, with that obtained with the XLD being slightly greater, but the timing for the onset of the diurnal jet was greatly increased using the XLD definition. The diurnal jet was overestimated using $\mathrm{MLD}_{0.1}$ while still lagging the current generated with XLD. Since the near surface shear increased linearly with time while the solar radiation increased as t^2 (for small t) it was not too surprising that the XLD reformed before the MLD, even for the smaller temperature threshold. What remains unclear is the exact timing for the reformation of the OSBL and the level of stratification necessary to decrease the constant stress layer at the onset of the diurnal jet.

At the onset of OSBL reformation, ε wasn't entirely a product of the wind stress input as convection can persist after the surface buoyancy flux changes on the order of 1 hour after sunrise (Callaghan et al. 2014). This suggests that even though an ε-based criterion for the OSBL definition yielded an OSBL reformation time to be 3 hours quicker than a temperature criterion, it may still lag the true constant stress layer depth on the order of 1 hour.

Both the MLD and XLD produce currents much larger than observations during the descent of the shear layer in the late afternoon. The descending H is mixing with the slower remnant layer below creating an additional source of drag. Introducing this entrainment into the momentum equations gives an improved agreement between the observed and modelled currents. Although including entrainment improves the timing of the diurnal jet, the magnitude is now less than what was observed. A summary of the magnitude and timing of the near surface currents is presented in Table 1. This underestimation of the diurnal jet most likely arises from the variability of τ and H from the composite day, but may also be due to the choice of r and that it may not be the same for the surface and remnant layers. The entrainment model also assumes there is no detrainment, i.e. $\partial H/\partial t > 0$, during the day. As the predominant mechanism for the shoaling of H is restratification and there is no momentum transfer associated with the discontinuous jump in H, this assumption of no detrainment appears valid.

Both diurnal and inertial motions play a role in the near surface dynamics during restratification. Since the inertial and diurnal periods are so close it has been difficult to differentiate the two processes. It is reasonable to expect a resonance type response at latitudes close to $\pm 30^\circ$ where the inertial and diurnal frequencies are identical. This would be analogous to the inertial resonance when τ varies close to the Coriolis frequency f (D'Asaro 1985). However, this interplay between the diurnal jet and inertial motions may still be greater at lower latitudes since the inertial period is greater and the wind stress and the surface currents are aligned for a greater duration.

These observations present new insight into the complicated processes associated with stable boundary layers. During conditions of low wind and high solar insolation an interesting feedback mechanism occurs which acts to increase mixing relative to the wind forcing. The enhanced stratification from the diurnal SST signal acts to limit the wind stress input to a shallow near surface layer which becomes unstable and mixes the warm upper layer with the remnant layer below. This process could be an important component to the air-sea transfer of momentum, heat and trace gases in tropical regions.

Acknowledgments. The authors are grateful for funding support from the National Science and Engineering Research Council of Canada from the scholarship PGSD3-410251-2011, the Office of Naval Research under award N62909-14-1-N296 and the Norwegian Research Council under PETROMAKS2 233901 project. LM thanks Olivier Peden and Olivier Ménage for their help with the Trèfle and A. Marsouin and P. Le Borgne from Météo-France for help in processing the radiative fluxes data. The Strasse cruise and data analysis was supported by LEFE/IMAGO and CNES/TOSCA grants.

APPENDIX A

Wind variability and the inertial model of D'Asaro (1985)

Phase averaged and mean values for the wind input are tested to assess the impact of wind variability on the inertial current response using (5). A mean latitude of 25.6°N is used for f. The inertial model is spun up for 12 days to achieve a quasi-steady state with LMT=0. The decay rate r is chosen to be $r = 0.15f$, consistent with previous studies (Alford 2001), giving a decay rate of $1/r = 7.8$ days. The currents are compared with the ADCP data averaged over the upper 5 metres.

Figure A1 shows the response of (5) to the composite day forcing. The three columns show the solutions to (5) for the various combinations of τ and H, where H is the $\mathrm{MLD}_{0.2}$. Using the observed time varying τ rather than a constant τ has little impact on the modeled currents. This suggests that the observed variability is predominantly due to the diurnal cycling of the boundary depth H.

APPENDIX B

Derivation of entrainment solution

At the onset of OSBL reformation, the remnant layer decouples from the surface stress and is free to propagate as a free inertial oscillation. Taking the upper layer of depth H and complex mean velocity Z and the remnant layer of depth $\hat{H}$ and complex mean velocity $\hat{Z}$, the momentum equations for both layers can be written as

$$\frac{\partial HZ}{\partial t} + \omega HZ = \frac{i\tau}{\rho} + \hat{Z}\frac{\partial H}{\partial t} \tag{B1}$$

$$\frac{\partial \hat{H}\hat{Z}}{\partial t} + \omega \hat{H}\hat{Z} = -\hat{Z}\frac{\partial H}{\partial t}, \tag{B2}$$

where the entrainment term $\hat{Z}\partial H/\partial t$ assumes the momentum in the remnant layer is transferred to the upper layer as the interface descends. Equations (B1) and (B2) ignore any interfacial friction between the two layers as this is expected to be much smaller in magnitude. Assuming a constant seasonal pycnocline depth, i.e. $H_0 = H + \hat{H}$ =constant, it is straightforward to derive (14) from (B2) assuming $\hat{H} \to 0$ as $\hat{Z} \to 0$. Adding (B1) and (B2) gives

$$\frac{\partial(HZ+\hat{H}\hat{Z})}{\partial t} + \omega(HZ+\hat{H}\hat{Z}) = \frac{i\tau}{\rho}. \tag{B3}$$

Equation (B3) states that the transport in the whole surface layer is equal to the Ekman transport $H_0 Z_E$, which is given for general τ by

$$H_0 Z_E = \int_{-\infty}^{t} \frac{i\tau(t')}{\rho} e^{-\omega(t-t')} dt' \tag{B4}$$

which is equal to (11) for constant τ and $H = H_0$.

Equation (14) states that the remnant layer is free from the direct influence of the surface stress and that its complex velocity evolves according to

$$\hat{Z}(t) = \hat{Z}(0)e^{-\omega t}. \tag{B5}$$

The composite daily cycle is assumed to begin at the instant of OSBL reformation, which we take as $t = 0$. At $t = 0$ the remnant layer velocity equals the OSBL velocity at the end of the previous day, hence $\hat{Z}(0) = Z(T_D)$, where T_D is the 24 hour period of the diurnal cycle. Furthermore, at $t = 0$ the surface and remnant layers have the same velocity, i.e .$\hat{Z}(0) = Z(0)$. Implementing these cyclic conditions give the solutions for the surface and remnant layers in (15) and (16) respectively.

References

Alford, M. H., 2001: Internal swell generation: The spatial distribution of energy flux from the wind to mixed layer near-inertial motions. *J. Phys. Oceanogr.*, **31 (8)**, 2359–2368.

Asher, W. E., A. T. Jessup, and D. Clark, 2014: Stable near-surface ocean salinity stratifications due to evaporation observed during STRASSE. *J. Geophys. Res. Oceans*, **119 (5)**, 3219–3233, doi:10.1002/2014JC009808.

Belcher, S. E., and Coauthors, 2012: A global perspective on Langmuir turbulence in the ocean surface boundary layer. *Geophys. Res. Lett.*, **39**, L18605, doi:10.1029/2012GL052932.

Bernie, D., S. Woolnough, J. Slingo, and E. Guilyardi, 2005: Modeling diurnal and intraseasonal variability of the ocean mixed layer. *J. Climate*, **18 (8)**, 1190–1202.

Brainerd, K., and M. Gregg, 1993: Diurnal restratification and turbulence in the oceanic surface mixed layer 1. Observations. *J. Geophys. Res.*, **98 (C12)**, 22 645–22 656.

Brainerd, K., and M. C. Gregg, 1995: Surface mixed and mixing layer depths. *Deep-Sea Res.*, **42 (9)**, 1521–1543.

Callaghan, A. H., B. Ward, and J. Vialard, 2014: Influence of surface forcing on near-surface and mixing layer turbulence in the tropical indian ocean. *Deep-Sea Res. Pt. I*, **94**, 107–123.

Clayson, C. A., and A. S. Bogdanoff, 2013: The effect of diurnal sea surface temperature warming on climatological air–sea fluxes. *J. Climate*, **26 (8)**, 2546–2556.

Cronin, M. F., and W. S. Kessler, 2009: Near-surface shear flow in the tropical pacific cold tongue front*. *J. Phys. Oceanogr.*, **39 (5)**, 1200–1215.

D'Asaro, E. A., 1985: The energy flux from the wind to near-inertial motions in the surface mixed layer. *J. Phys. Oceanogr.*, **15 (8)**, 1043–1059.

D'Asaro, E. A., 2014: Turbulence in the upper-ocean mixed layer. *Annu. Rev. Mar. Sci.*, **6**, 101–115.

de Boyer Montégut, C., G. Madec, A. S. Fischer, A. Lazar, and D. Iudicone, 2004: Mixed layer depth over the global ocean: An examination of profile data and a profile-based climatology. *J. Geophys. Res.*, **109**, C12003, doi:10.1029/2006JC004051.

Drushka, K., S. T. Gille, and J. Sprintall, 2014: The diurnal salinity cycle in the tropics. *J. Geophys. Res. Oceans*, **119 (9)**, 5874–5890, doi:10.1002/2014JC009924.

Fairall, C. W., E. F. Bradley, J. E. Hare, A. A. Grachev, and J. B. Edson, 2003: Bulk parameterization of air-sea fluxes: Updates and verification for the COARE algorithm. *J. Climate*, **16**, 571–591.

Fer, I., and A. Sundfjord, 2007: Observations of upper ocean boundary layer dynamics in the marginal ice zone. *J. Geophys. Res.*, **112**, C04012, doi:10.1029/2005JC003428.

Gargett, A. E., and C. E. Grosch, 2014: Turbulence process domination under the combined forcings of wind stress, the langmuir vortex force and surface cooling. *J. Phys. Oceanogr.*, **44**, 44–67.

Kara, A. B., P. A. Rochford, and H. E. Hurlburt, 2000: An optimal method for ocean mixed layer depth. *J. Geophys. Res.*, **105 (C7)**, 16 803–16 821.

Kawai, Y., and A. Wada, 2007: Diurnal sea surface temperature variation and its impact on the atmosphere and ocean: A review. *J. Oceanogr.*, **63 (5)**, 721–744.

Kenyon, K. E., 1969: Stokes drift for random gravity waves. *J. Geophys. Res.*, **74 (28)**, 6991–6994.

Kudryavtsev, V. N., and A. V. Soloviev, 1990: Slippery near-surface layer of the ocean arising due to daytime solar heating. *J. Phys. Oceanogr.*, **20**, 617–628.

Large, W. G., J. C. McWilliams, and S. C. Doney, 1994: Ocean vertical mixing: A review and a model with a nonlocal boundary layer parameterization. *Rev. of Geophys.*, **32 (4)**, 363–403.

Lombardo, C. P., and M. C. Gregg, 1989: Similarity scaling of viscous and thermal dissipation in a convecting surface boundary layer. *J. Geophys. Res.*, **94 (C5)**, 6273–6284.

Lozovatsky, I. D., E. Roget, H. J. S. Fernando, M. Figueroa, and S. Shapovalov, 2006: Sheared turbulence in a weakly stratified upper ocean. *Deep-Sea Res. Pt. I*, **53**, 387–407.

McWilliams, J. C., P. P. Sullivan, and C. H. Moeng, 1997: Langmuir turbulence in the ocean. *J. Fluid Mech.*, **334**, 1–30.

Mellor, G., 2001: One-dimensional, ocean surface layer modeling: A problem and a solution. *J. Phys. Oceanogr.*, **31**, 790–809.

Miles, J., 1961: On the stability of heterogeneous shear flows. *J. Fluid Mech.*, **10**, 496–508.

Nicholson, D. P., S. T. Wilson, S. C. Doney, and D. M. Karl, 2015: Quantifying subtropical North Pacific gyre mixed layer primary productivity from Seaglider observations of diel oxygen cycles. *Geophys. Res. Lett.*, **42**, 4032–4039, doi:10.1002/2015GL063065.

Plueddemann, A. J., and R. A. Weller, 1999: Structure and evolution o the oceanic surface boundary layer during the surface waves processes program. *Journal of Marine Systems*, **21**, 85–102.

Pollard, R. T., and R. Millard, 1970: Comparison betwen observed and simulated wind-generated inertial oscillations. *Deep-Sea Res.*, **17 (4)**, 813–821.

Price, J. F., R. A. Weller, and R. Pinkel, 1986: Diurnal cycling: Observations and models of the upper ocean response to diurnal heating, cooling, and wind mixing. *J. Geophys. Res.*, **91 (C7)**, 8411–8427.

Rascle, N., F. Ardhuin, and E. A. Terray, 2006: Drift and mixing under the ocean surface: A coherent one-dimensional description with application to unstratified conditions. *J. Geophys. Res.*, C03016, doi:10.1029/2005JC003004.

Reverdin, G., and Coauthors, 2015: Surface salinity in the North Atlantic subtropical gyre: During the STRASSE/SPURS summer 2012 cruise. *Oceanography*, **28 (1)**, 114–123.

Shay, T. J., and M. C. Gregg, 1986: Convectively driven turbulent mixing in the upper ocean. *J. Phys. Oceanogr.*, **16**, 1777–1798.

Smyth, W., J. Moum, L. Li, and S. Thorpe, 2013: Diurnal shear instability, the descent of the surface shear layer, and the deep cycle of equatorial turbulence. *J. Phys. Oceanogr.*, **43 (11)**, 2432–2455.

Stevens, C., B. Ward, C. Law, and M. Walkington, 2011: Surface layer mixing during the SAGE ocean fertilization experiment. *Deep-Sea Res. Pt. II*, **58 (6)**, 776–785.

Sutherland, G., K. H. Christensen, and B. Ward, 2014a: Evaluating Langmuir turbulence parameterizations in the ocean surface boundary layer. *J. Geophys. Res. Oceans*, **119**, 1899–1910, doi:10.1002/2013JC009537.

Sutherland, G., G. Reverdin, L. Marié, and B. Ward, 2014b: Mixed and mixing layer depths in the ocean surface boundary layer: Buoyancy-driven conditions. *Geophys. Res. Lett.*, **41**, 8469–8476, doi:10.1002/2014GL061939.

Sutherland, G., B. Ward, and K. H. Christensen, 2013: Wave-turbulence scaling in the ocean mixed layer. *Ocean Sci.*, **9**, 597–608.

Terray, E. A., M. A. Donelan, Y. C. Agrawal, W. M. Drennan, K. K. Kahma, A. J. Williams III, P. A. Hwang, and S. A. Kitaigorodskii, 1996: Estimates of kinetic energy dissipation under breaking waves. *J. Phys. Oceanogr.*, **26**, 792–807.

Vagle, S., J. Gemmrich, and H. Czerski, 2012: Reduced upper ocean turbulence and changes to bubble size distributions during large downward heat flux events. *J. Geophys. Res.*, **117 (C7)**.

Wain, D. J., J. M. Lilly, A. H. Callaghan, I. Yashayaev, and B. Ward, 2015: A breaking internal wave in the surface ocean boundary layer. *J. Geophys. Res. Oceans*, **120**, 4151–4161, doi:10.1002/2014JC010416.

Ward, B., 2006: Near-surface ocean temperature. *J. Geophys. Res.*, **111**, doi:10.1029/2004JC002689.

Ward, B., T. Fristedt, A. H. Callaghan, G. Sutherland, X. Sanchez, J. Vialard, and A. ten Doeschate, 2014: The Air-Sea Interaction Profiler (ASIP): An autonomous upwardly-rising profiler for microstructure measurements in the upper ocean. *J. Atmos. Oceanic Technol.*, **31 (10)**, 2246–2267.

Webb, A., and B. Fox-Kemper, 2011: Wave spectral moments and Stokes drift estimation. *Ocean Modelling*, **40 (3-4)**, 273–288.

Weller, R. A., S. Majumder, and A. Tandon, 2014: Diurnal restratification events in the southeast pacific trade wind regime. *J. Phys. Oceanogr.*, **44**, 2569–2587.

Weller, R. A., and A. J. Plueddemann, 1996: Observations of the vertical structure of the oceanic boundary layer. *J. Geophys. Res.*, **101 (C4)**, 8789–8806.

Woods, J. D., and V. Strass, 1986: The response of the upper ocean to solar heating. II: The wind-driven current. *Quart. J. Roy. Meteor. Soc.*, **112**, 29–42.

LIST OF TABLES

TABLE 1. Magnitude and time of peak along-wind (v), cross-wind (u) and magnitude (z) of the observed mixed layer currents relative to 40 m depth. Simulated currents using various definitions for the OSBL depth are presented relative to the observed value. The superscript ^{1} denotes the damped slab layer of (5) while ^{2} denotes the two layer slab model of (15).

Model	max(v); time cm s^{-1}; LMT	max(u); time cm s^{-}1;LMT	max(z); time cm s^{-1}; LMT
OBS	10.4; 13:30	11.2; 18:30	13.6; 14:30
XLD^1	-2.1; +2:00	+0.3; +3:00	-1.8; +6:00
MLD$^1_{0.2}$	-1.5; +3:00	-0.8; +4:00	-2.7; +6:00
MLD$^1_{0.1}$	+8.9; +4:00	+10.6; +5:00	+9.6; +6:00
XLD^2	-2.0; +1:00	-2.2; +1:00	-2.4; $\pm$0:00
MLD$^2_{0.2}$	-4.5; +2:00	-4.6; -1:00	-5.5; +1:00
MLD$^2_{0.1}$	+4.5; +6:00	+0.4; +2:00	+3.0; +5:00

LIST OF FIGURES

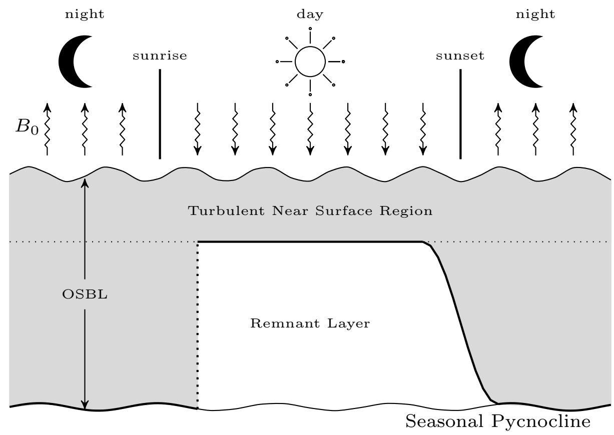

FIG. 1. A schematic depicting the diurnal cycle of turbulence. The shaded region represents the OSBL.

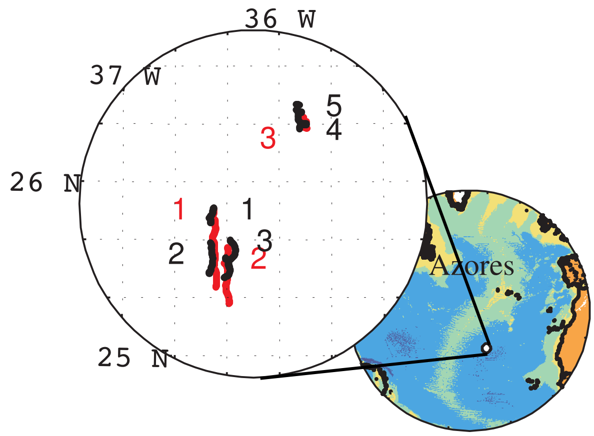

FIG. 2. Location for the five ASIP deployments(shown in black) and three Trèfle deployments (shown in red) during late August / early September 2012.

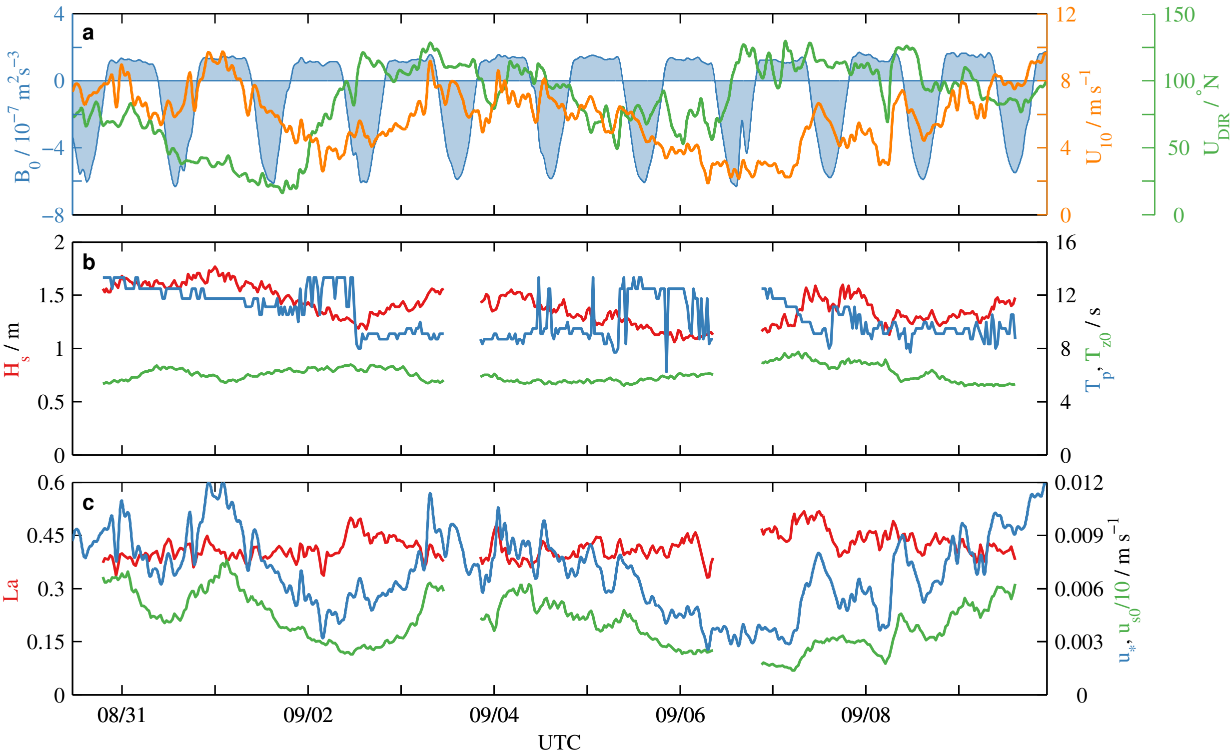

FIG. 3. Time series of observations of (a) surface buoyancy flux B_0 (blue), wind speed U_{10} (orange) and direction U_{DIR} (green) (b) significant wave height H_s (red), peak period T_p (blue) and zero up crossing period T_z (green) and (c) the turbulent Langmuir number La (red) as well as the friction velocity u_* (blue) and the surface Stokes drift/10 $u_{s0}/10$ (green).

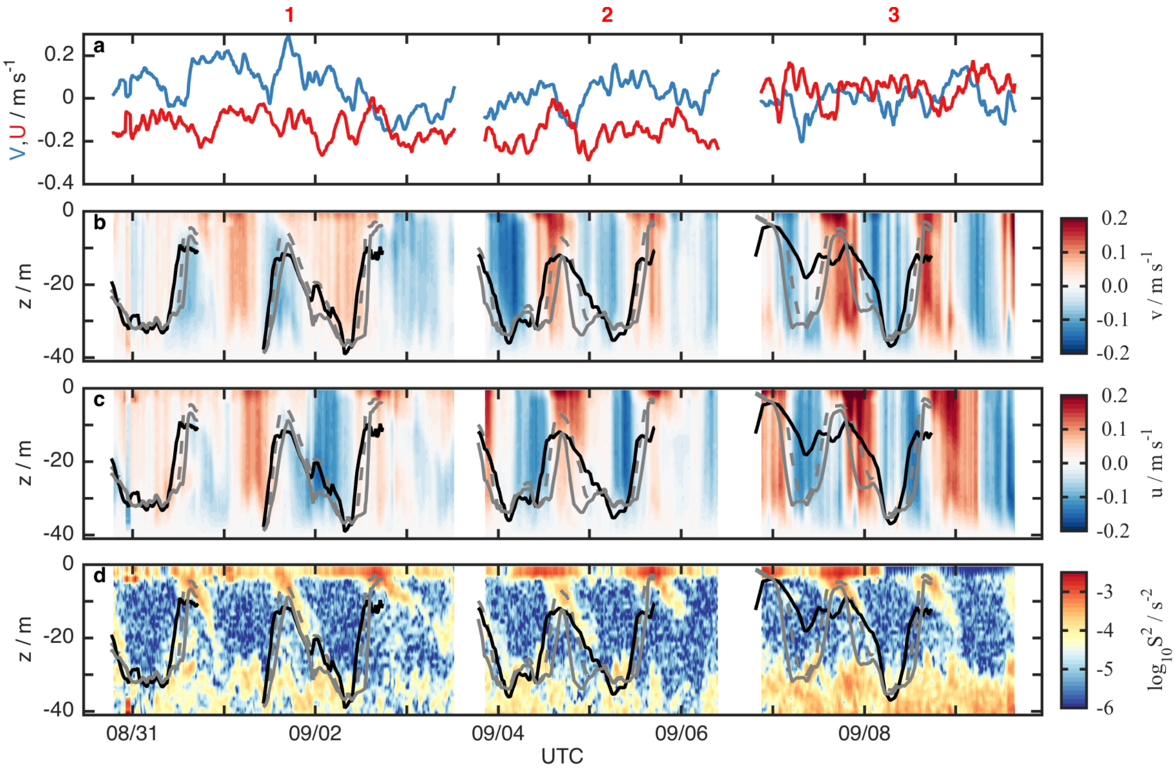

639 FIG. 4. Observations of near surface currents from each of the three Trèfle deployments, deployment numbers are along the top of the figure, of (a) the mean velocity at 40 m, the (b) along-wind and (c) cross-wind components of the velocity relative to 40 m and (d) the shear squared. The black line denotes the XLD and the solid and dashed grey lines denote the MLD calculated using $\Delta T = 0.2$ and $0.1°C$ respectively.

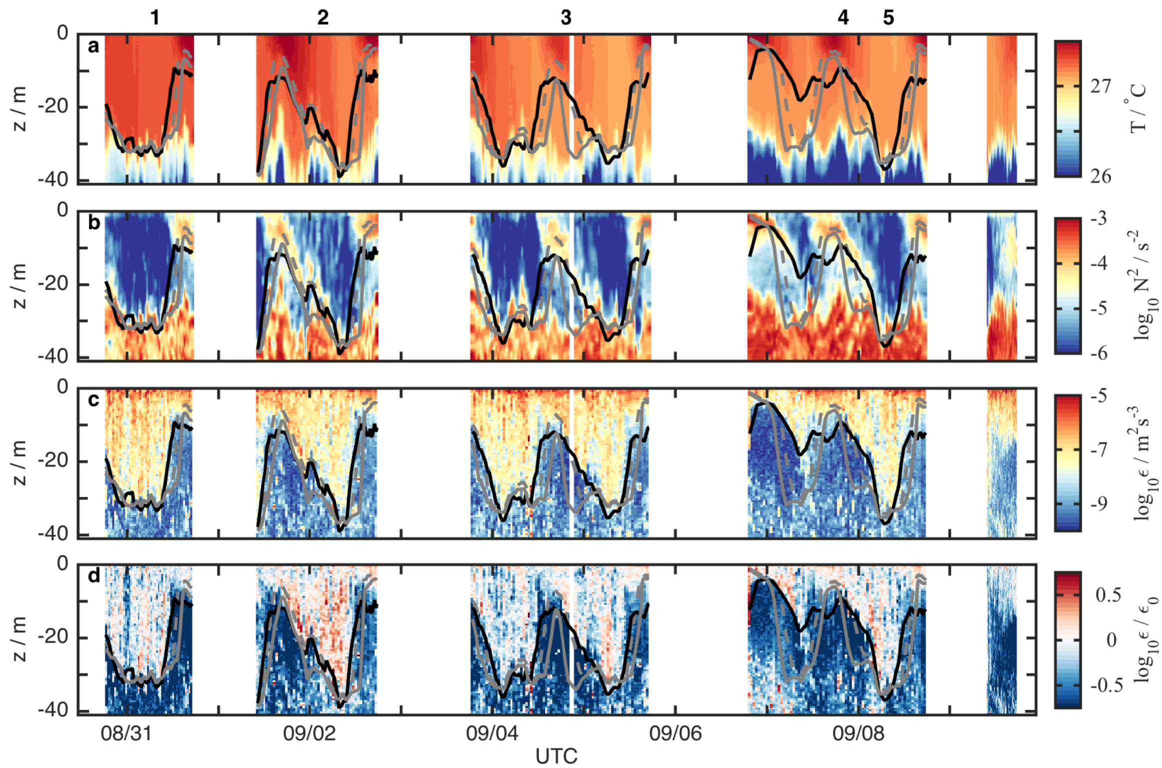

643 FIG. 5. Observations from the five ASIP deployments, deployment numbers are along the top of the figure, of (a) temperature, (b) stratification, (c) turbulent dissipation rate ε and (d) normalized turbulent dissipation rate $\varepsilon/\varepsilon_0$. The black line denotes the XLD and the solid and dashed grey lines denote the MLD calculated using $\Delta T = 0.2$ and $0.1°$C respectively.

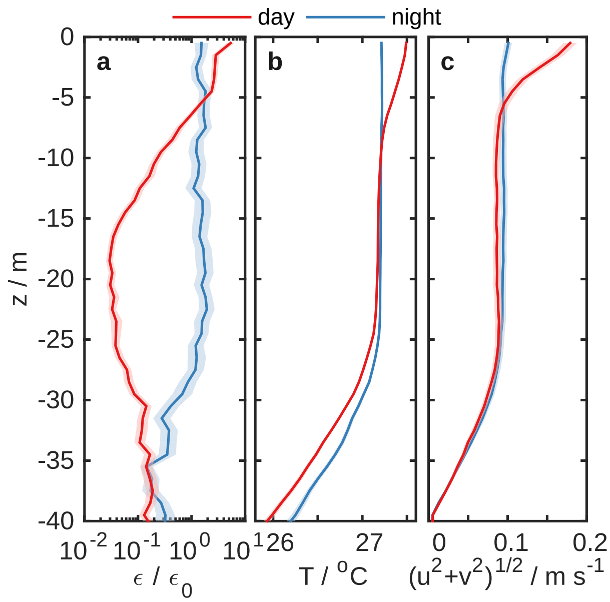

FIG. 6. Mean day and night profiles of (a) normalized dissipation rate, (b) temperature, and (c) velocity magnitude. Night is defined between 01:00 and 04:00 LMT and day is 13:00 to 16:00 LMT. Shaded regions represent 95% confidence intervals as calculated with a bootstrap method.

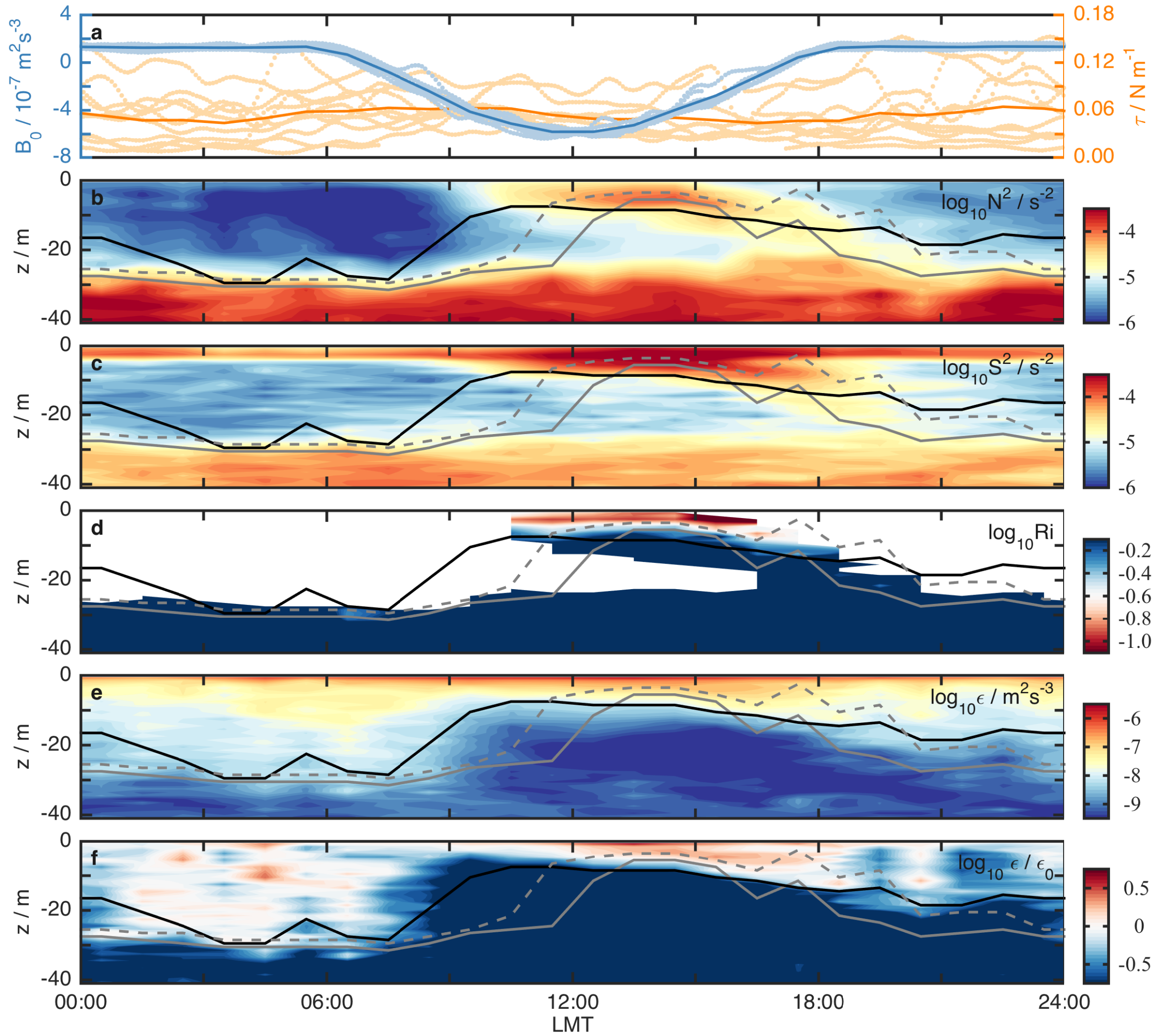

FIG. 7. Composite day for (a) B_0 (blue) and τ (orange), (b) N^2, (c) S^2, (d) Ri_b, (e) ε and (f) $\varepsilon/\varepsilon_0$. The black line in panels b-f is the XLD and the solid and dashed grey lines are the MLD calculated with $\Delta T = 0.2$ and 0.1°C respectively.

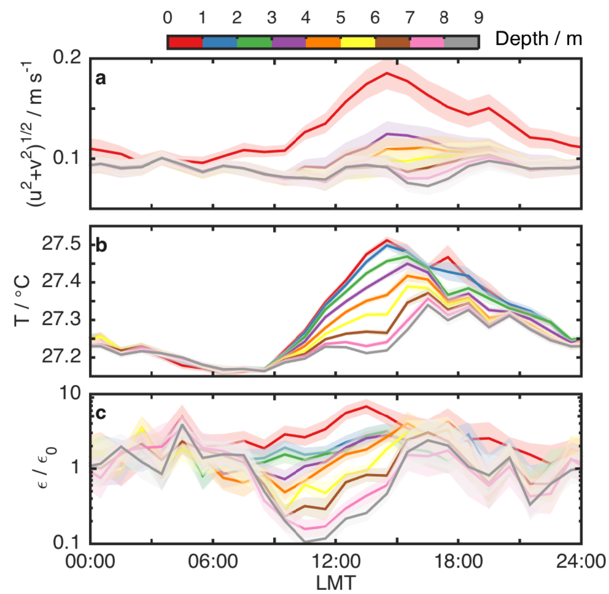

FIG. 8. Depth averaged composite day for (a) magnitude of surface velocity, (b) temperature and (c) $\varepsilon/\varepsilon_0$ for the upper 9 metres. The shaded regions denote 95% confidence intervals for each depth level calculated using a bootstrap method.

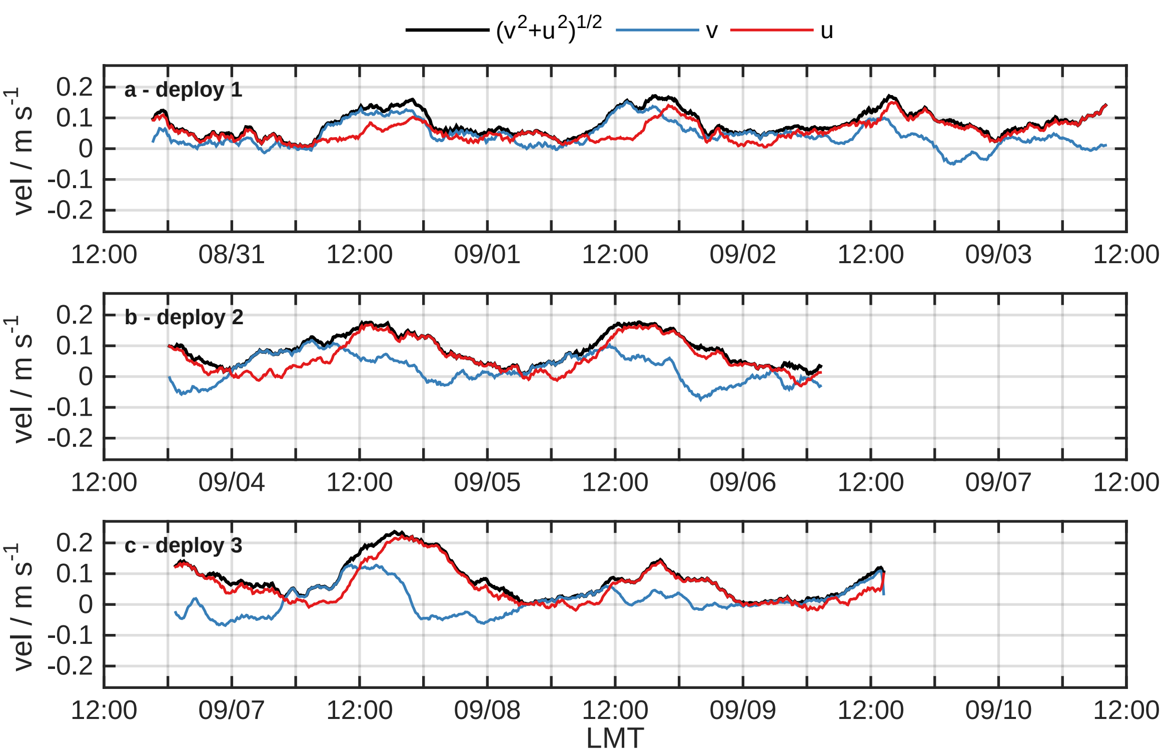

656 FIG. 9. Diurnal jet calculated from the observed velocity at 0.5 m relative to the velocity at 20 m where v and
657 u are the along-wind and cross-wind components of respectively.

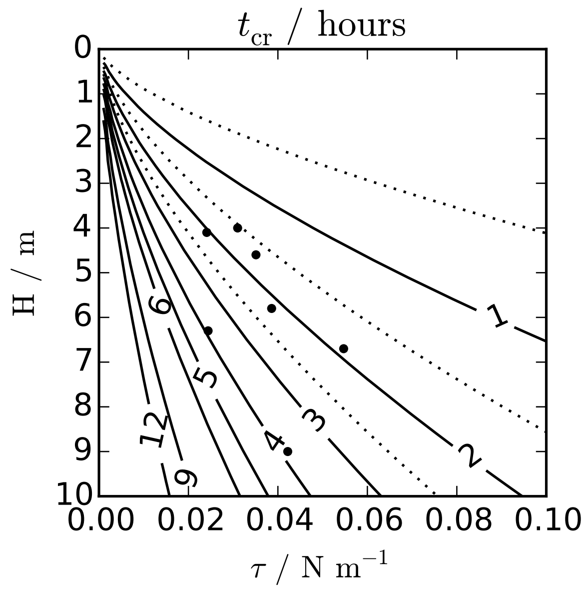

658 FIG. 10. Contours of the time it takes for $\mathrm{Ri}_b = \mathrm{Ri}_{cr}$ calculated from (9). The black dots denote observations
659 of H and τ.

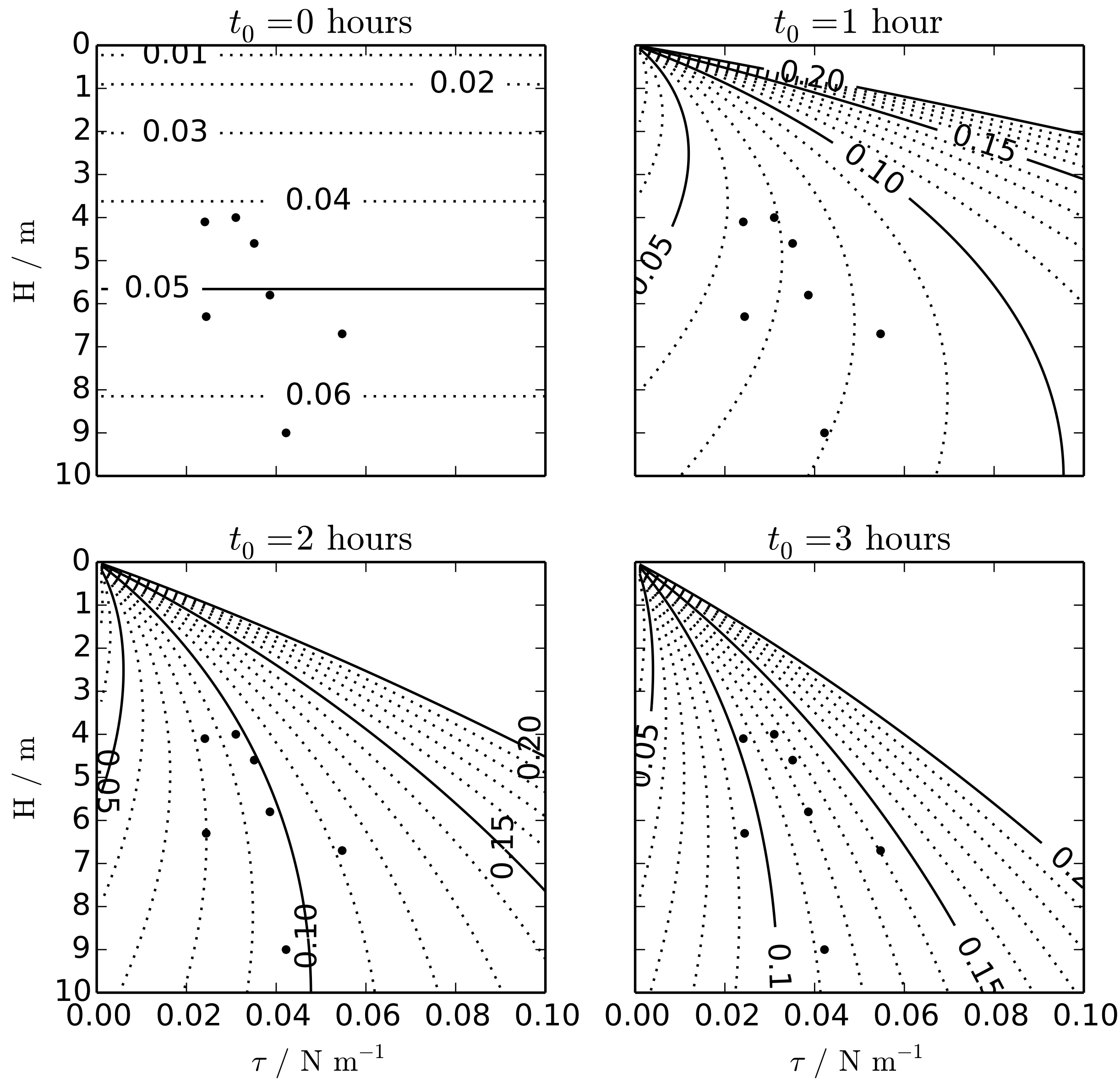

660 FIG. 11. Diurnal jet amplitude assuming the t_{cr} of Fig. 10 for different values of t_0. The black dots denote
661 observations of H and τ.

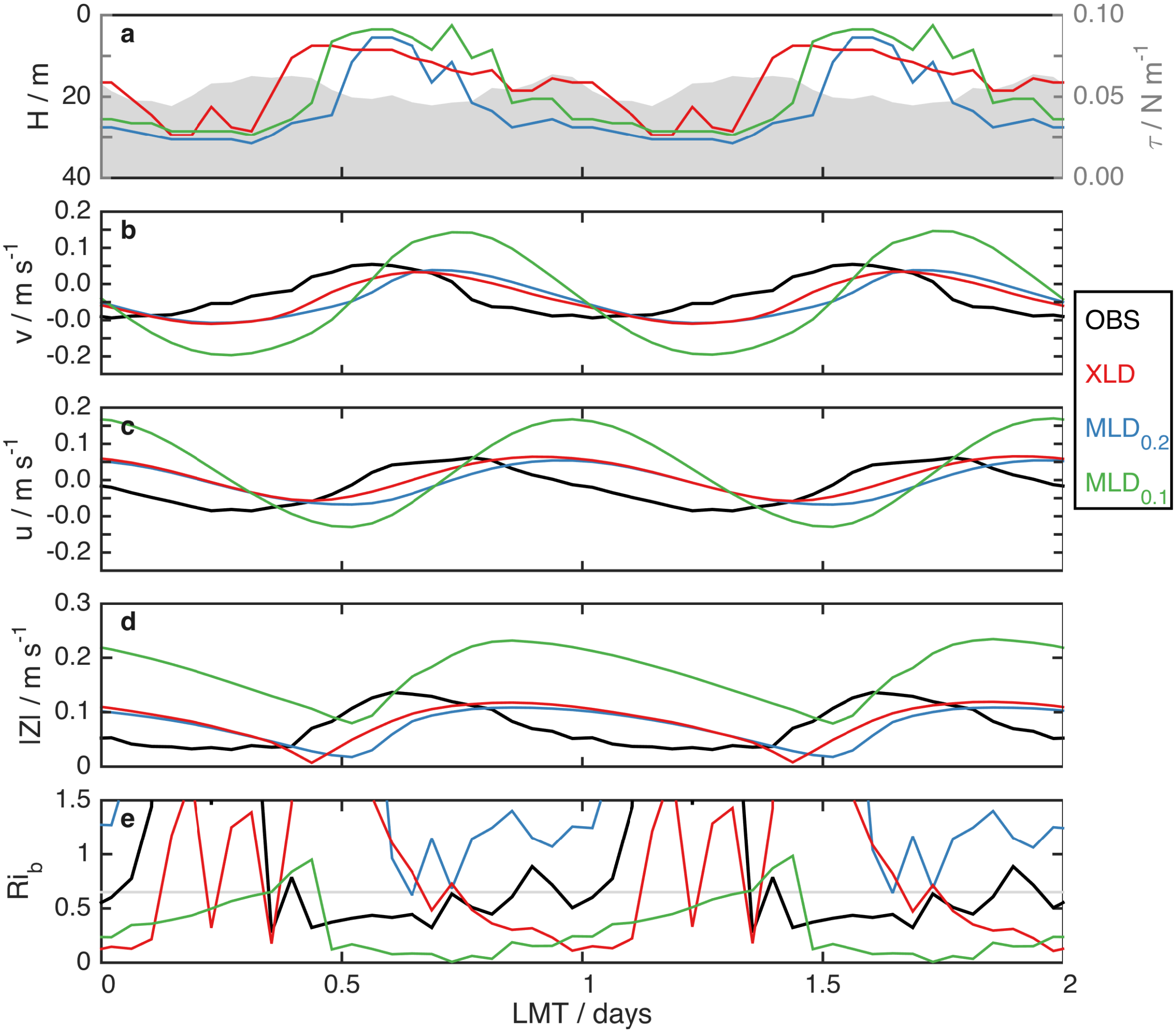

FIG. 12. Quasi-steady state surface currents from observations (Z_0, black), and from (5) using the XLD (red) and the MLD using a $\Delta T = 0.2^\circ$ C threshold (blue) and a $\Delta T = 0.1^\circ$ C threshold (green).

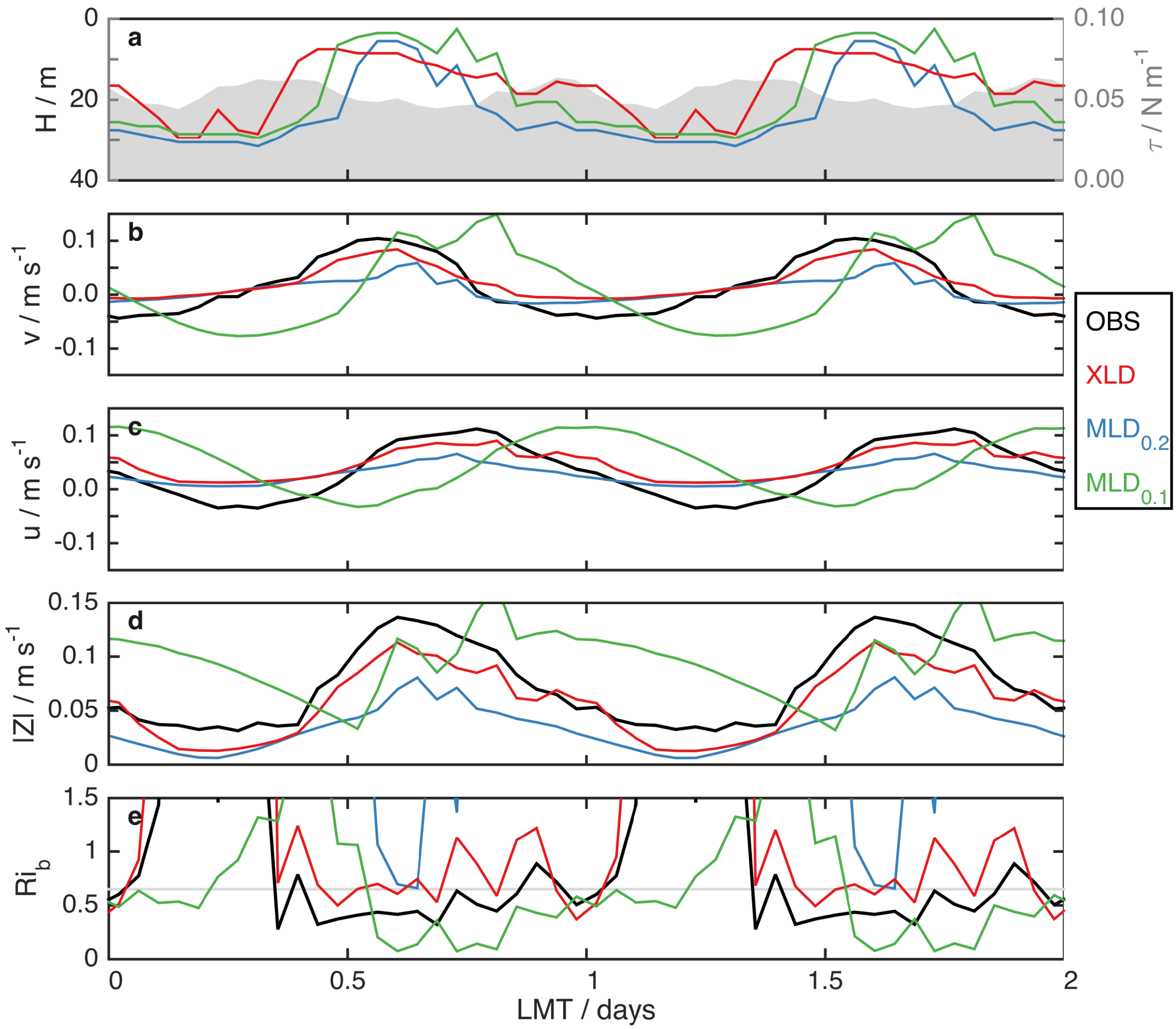

FIG. 13. Same as Fig. 12 but using (13) which includes the effect of entrainment.

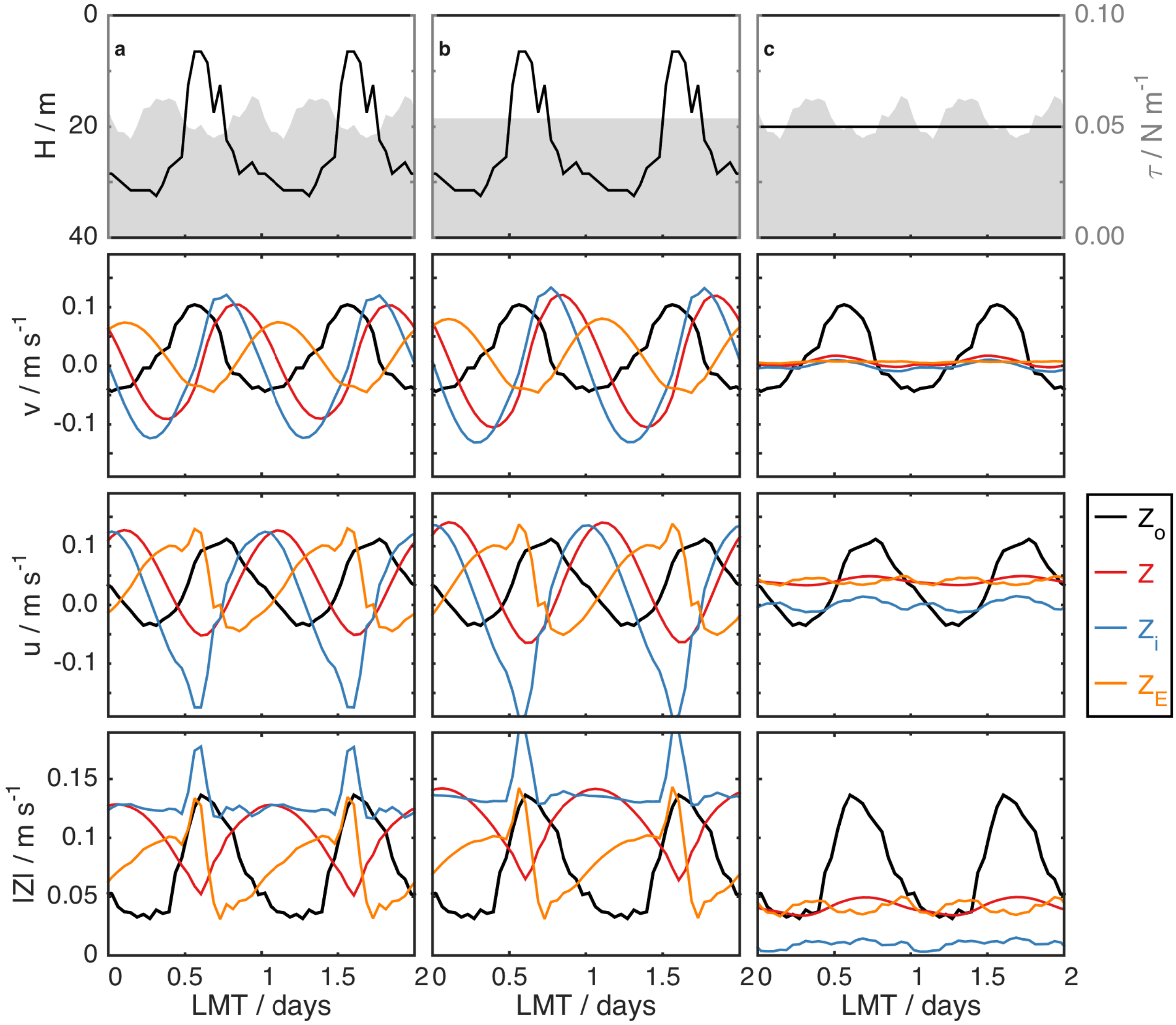

664 Fig. A1. Quasi-steady state surface currents from observations (Z_0, black), as well as total current (Z, red), inertial (Z_I, blue) and Ekman (Z_E, orange) currents generated with (5) and (a) τ and $\mathrm{MLD}_{0.2}$, (b) $\overline{\tau}$ and $\mathrm{MLD}_{0.2}$ and (c) τ and $H = 20$m.